

PCCP

Accepted Manuscript



This is an *Accepted Manuscript*, which has been through the Royal Society of Chemistry peer review process and has been accepted for publication.

Accepted Manuscripts are published online shortly after acceptance, before technical editing, formatting and proof reading. Using this free service, authors can make their results available to the community, in citable form, before we publish the edited article. We will replace this *Accepted Manuscript* with the edited and formatted *Advance Article* as soon as it is available.

You can find more information about *Accepted Manuscripts* in the [Information for Authors](#).

Please note that technical editing may introduce minor changes to the text and/or graphics, which may alter content. The journal's standard [Terms & Conditions](#) and the [Ethical guidelines](#) still apply. In no event shall the Royal Society of Chemistry be held responsible for any errors or omissions in this *Accepted Manuscript* or any consequences arising from the use of any information it contains.

Cite this: DOI: 10.1039/c0xx00000x

www.rsc.org/xxxxxx

ARTICLE TYPE

Unraveling the role of La A-site substitution on oxygen ion diffusion and oxygen catalysis in perovskite BaFeO₃ by data-mining molecular dynamics and density functional theory

Chi Chen,^a Zarah Medina Baiyee^a and Francesco Ciucci^{a,b}

⁵ Received (in XXX, XXX) Xth XXXXXXXXX 20XX, Accepted Xth XXXXXXXXX 20XX
DOI: 10.1039/b000000x

BaFeO₃ (BFO) is a promising parent material for high-temperature oxygen catalysis. The effects of La substitution on the oxygen ion diffusion and oxygen catalysis in A-site La-substituted BFO are studied by combining data-driven molecular dynamics (MD) simulations and density functional theory (DFT) calculations. The data-driven MD simulations are capable of providing atomic level information regarding oxygen jumps at different sites, bridging the resolution gap of analysis between MD and DFT. The simulations identify several effects due to the introduction of La. First, according to simple electroneutrality considerations and DFT calculations, La tends to decrease the concentration of oxygen vacancies in BFO. Second, La substitution lowers the activation energy of local oxygen migration, providing faster paths for oxygen diffusion. The MD analysis predicts a higher hopping rate through La-containing bottlenecks as well as easier oxygen jumps from the La-rich cages and lower dwell times of oxygen in those cages. DFT calculations confirm a lower migration energy through La-containing bottlenecks. Third, the electrocatalytic activity of the material decreases with La, as indicated by a lower O p-band center and higher oxygen vacancy formation energies.

20 Introduction

Mixed ionic-electronic conductors have been applied as oxygen transport membranes¹, electrode materials for solid oxide fuel cells (SOFCs)²⁻⁴, and water splitting catalysts⁵. Owing to their good ionic and electronic conductivity, outstanding ability to catalyze oxygen reaction and relatively low price, ceramic materials based on perovskite-type BaFeO₃ (BFO) have attracted considerable attention.⁶⁻⁹ From a materials design point of view, Ba has a large cation radius, which leads to a high tolerance factor and potentially higher symmetry lattices when the B site is occupied by large cations. Indeed, oxygen vacancy disordered cubic phases are commonly observed in BFO-based perovskites. In addition, the B-site cation Fe, with variable valence states, provides active oxygen catalysis sites and enables electronic conduction via Fe-O-Fe linkages.

A large body of research has been devoted to studying BFO-related materials. Amongst them, one noticeable material is Ba_{0.5}Sr_{0.5}Co_{0.8}Fe_{0.2}O_{3-δ} (BSCF), possibly the most influential perovskite catalyst in SOFCs^{10,11}. There are numerous studies on the use of BFO perovskites, yet most of these materials contain a small or considerable amount of substitution of cationic elements due to the need to stabilize the cubic phase structure. It was previously reported that BFO synthesized by conventional methods exhibits mixed phases,⁸ where only the cubic phase retains disordered oxygen vacancies and has the ability to conduct oxygen ions at a relatively high rate. The monoclinic phase has ordered oxygen vacancies¹², which are detrimental to

oxygen conduction. Unfortunately, it is difficult to synthesize stoichiometric cubic BFO because the high valence Fe⁴⁺ is not favorable in this system since the Fe 3d band energy is lower than O 2p band, introducing a negative ligand to metal charge transfer energy.¹³ Although phase transition of the mixed phase to pure cubic structure is observed at around 900 °C,¹⁴ application of this material at intermediate temperature is not feasible because the material performance substantially decreases due to the presence of the vacancy-ordered monoclinic phase. Nevertheless, several synthesis methods have been used to obtain phase-pure cubic BFO at relatively low temperatures. For example, the cubic phase of BFO has been successfully deposited as thin films on SrTiO₃ by pulsed laser deposition.¹⁵⁻¹⁷ In addition, cubic BFO can be obtained by first reducing the material at high temperature to form the pure hexagonal phase, followed by oxidation in ozone at 200 °C.¹⁸ The temperature is kept low in order to avoid high temperature reduction of the transition metal. Additionally, electrochemical methods can be used to oxidize BFO in order to obtain a cubic phase.¹⁹ However, the practical applications of those synthesis methods are limited because the working temperature of SOFCs or oxygen transport membranes is much higher than the conditions of synthesis. Nevertheless, doping is a simple, yet effective method to obtain the cubic phase. Materials obtained by such methods usually show greater stability in a broader range of conditions. Hence, research efforts have been undertaken to stabilize the cubic phase by selective doping of cations into the A site, e.g., La,^{6-8, 20-22} or into the B site, e.g., Zr²³, Y²⁴, Ce²⁵, Cu or Ni²⁶, Nb²⁷ and In²⁸, where the design strategy often aims at driving the Goldschmidt tolerance factor

closer to unity²⁹. It should be noted that in perovskites, the B-site metal provides electronic conducting pathways and also the reaction sites for oxygen adsorption.³⁰ For this reason, it is important to have metal cations with variable valence states at the B site to ensure good electronic conductivity as well as good oxygen adsorption. Unfortunately, elements that work well as cubic phase stabilizers usually have a fixed valence state, e.g., Zr⁴⁺ and Y³⁺.^{23, 24, 27} Hence, the substitution of Fe with fixed valence state cations as a strategy to stabilize the cubic phase structure may hinder the electronic conductivity and electrocatalytic activity of the material. As a consequence A-site doping may be more beneficial and in this work, A-site substitution is studied. Specifically, this article focuses on La substitution because it is characterized by the highest oxygen permeation among other A-site doped BFO materials³¹ and by a low polarization resistance when La-doped BFO is used as a cathode in SOFCs^{6, 8, 20}.

In this article, the role of A-site La substitution on BFO, in relation to oxygen ion diffusion and oxygen catalysis, is investigated in detail by MD simulations and DFT calculations. Our previous MD simulations found that the oxygen diffusivity decreased with increasing La content, primarily due to the decrease of oxygen vacancy concentration⁶. Therein, we employed a simple conventional approach to analyze oxygen diffusion, i.e., the oxygen diffusivity was calculated by fitting the mean-squared displacements (MSDs). This approach however, may not be compared directly with higher level calculations such as DFT. For example, recent DFT calculations of the La_{1-x}Sr_xCo_{1-y}Fe_yO_{3-δ} have shown that the oxygen vacancy formation is more favorable near La³⁺ in comparison to Sr²⁺, contradicting the conclusion that one could draw from considering only the coulombic interactions.³² The apparent disagreement stems from the conventional analysis of MD simulations; by only computing the MSD one is unable to obtain detailed information regarding atomic-level oxygen hopping. The study of Mastrikov et al.³² also pointed out that the local cation configuration affects the oxygen transport barrier, as was also suggested by other authors.³³ For this reason, the analysis of local oxygen jumps in MD simulations may be beneficial for elucidating the diffusion mechanisms and linking these insights with DFT simulations.

We recently developed a machine learning framework for performing the large-scale analysis of oxygen atom hops.³⁴ The work highlighted the necessity of studying in greater detail the impact of local cation environment on the diffusion behavior. In the current work, this data mining approach is applied for the first time to study the impact of dopants. Oxygen hops in the lattice from different local cationic arrangement can be counted and the dwell time analysis of oxygen at different sites is performed. We show that the contradictions between the MD and the DFT approach can be rationalized once more information is obtained from the MD simulations.

Methods

MD simulations and data analysis

Molecular dynamics simulations were carried out in LAMMPS.³⁵ The interactions between ions were described by the Buckingham pairwise potential model,^{36, 37} with the parameters and methods

taken from our previous work.⁶ 8x8x10 supercells of Ba_{1-x}La_xFeO_{2.5+x/2} (x = 0.1, 0.2, 0.3, 0.4 and 0.5) were studied. Here, we discuss the x = 0.5 case, as at this level the even La and Ba cation ratio enables a straightforward comparison of the effect of the A-site cation. The supplementary information contains the results of other substitution levels. The experimentally applied 5% doping was not studied as this case approaches the La-free system. For each substitution level, we randomly generated 7 different cation/vacancy configurations. We performed test calculations and found 7 configurations sufficient to give consistent results with further increasing this number. Temperatures were ramped from 1173 K to 1573 K with a 100 K step. During each simulation, the system was first equilibrated in the NPT ensemble for 100 ps, followed by a 2 ns data collection run in the NVT ensemble. The Noose-Hover thermostat was applied to control the temperatures. The ion trajectories were output every 1 ps, resulting in the total data size of approximately 40 Gb for all the output trajectories.

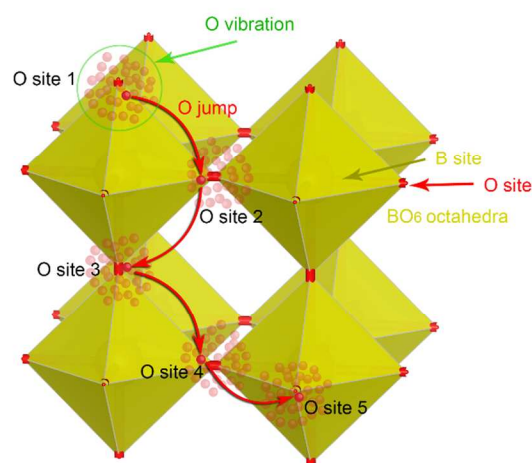


Fig. 1 Schematic of oxygen movement through the lattice. The oxygen movement involves both the vibration around the lattice sites (shown in green circles) and the migration between lattice sites (shown as red arrows).

As schematically illustrated in **Fig. 1**, the oxygen anions primarily vibrate around their equilibrium position, and occasionally jump to neighboring vacant oxygen sites. To understand the diffusion mechanism and the impact of the local cation environment on diffusion, it is necessary to study in-depth the oxygen jump behavior. However there are several challenges in this type of study. First, it is difficult to ascribe oxygen atoms to a certain site due to their random movements at elevated temperature. Second, it is nontrivial to identify the jump events. However, using machine-learning analysis, the individual oxygen jump event between different sites can be determined. In addition to obtaining the number of hopping events, we can also estimate the time at which the oxygen jumps occur and the nature of the hopping events, as illustrated in **Fig. 1**. Naturally, the hopping frequency as well as the dwell time of sites can be obtained. Furthermore, the location of oxygen is characterized by its surrounding cations. Obtaining information regarding oxygen jumps and the residence time at certain locations helps explain the oxygen transport mechanism. From this, we can identify the most favorable diffusion pathways and attempt to help design the

materials.

DFT calculations

Spin polarized DFT calculations were carried out using VASP with plane wave basis sets.^{38, 39} All the calculations used the PBE-GGA pseudopotentials with the soft potential specifically used for oxygen due to its low cut-off energy. In addition, we adopted the DFT+U approach, and took an effective Hubbard U parameter as 4 eV for Fe.^{40, 41} The electronic energy tolerance was set to 10^{-5} eV and the force tolerance for the structural relaxation was 0.02 eV/Å. The model system consisted of a $2 \times 2 \times 2$ cell, with a total of 40 atoms. Furthermore, $4 \times 4 \times 4$ MP k-point meshes were used for the normal calculations, and the grid density was doubled in calculating the density of state (DOS) by the tetrahedron method.⁴² In the computations, the system was first fully relaxed with freely adjustable lattice parameters as well as ion positions. The defect calculations were then carried out at fixed lattice parameters as obtained from the relaxations. The migration enthalpy of oxygen in the lattice was computed by the climbing image nudged elastic band theory as implemented in the vtst tools.⁴³ Three intermediate images were computed with the spring constant of -5 eV/Å². The structure was visualized using the VESTA software.⁴⁴

Results and discussion

Oxygen migration analysis

In an ABO₃ perovskite lattice, an oxygen atom is located in an octahedral hole surrounded by 4 A-site cations and 2 B-site cations. In the case of doped BFO, Fe is the only B site element, and so the different oxygen sites can only be distinguished by the variation of surrounding A-site cation configuration. As a result, five different types of oxygen cages can be found and are denoted as c_1 (BaBaBaBa), c_2 (BaBaBaLa), c_3 (BaBaLaLa), c_4 (BaLaLaLa) and c_5 (LaLaLaLa) where the subscript is the number of La atoms in the cage plus 1, as shown in Fig. 2. For an oxygen jump between two cages, it passes through bottlenecks formed by 2 A-site cations and 1 B-site cation. As a result, three different bottlenecks can be identified and are designated as b_1 (BaBaFe), b_2 (BaLaFe) and b_3 (LaLaFe), as also shown in Fig. 2.

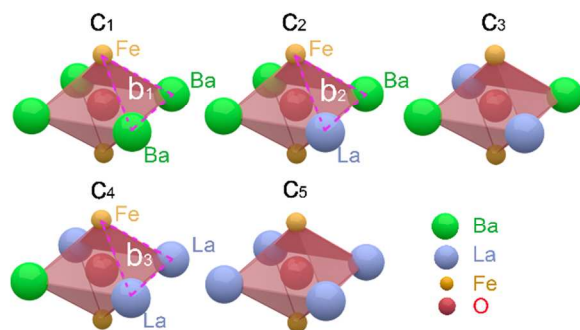


Fig. 2 Depiction of the oxygen cages and migration bottlenecks.

The substitution fractions of La are $x = 0.1, 0.2, 0.3, 0.4$ and 0.5 in $\text{Ba}_{1-x}\text{La}_x\text{FeO}_{3-\delta}$. For different substitution fractions, the number of different oxygen site types is shown in Fig. 3.

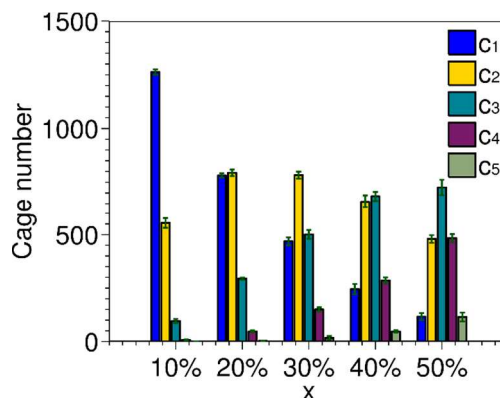


Fig. 3 The number of different cages for different La substitution fractions x in $8 \times 8 \times 10$ supercells of $\text{Ba}_{1-x}\text{La}_x\text{FeO}_{3-\delta}$. The error bars are the standard deviations of cage numbers from 7 different configurations.

As expected, the number of c_1 cages is the highest for low La fractions and this number decreases with increasing La content. In addition, small error bars are observed from taking 7 configurations, as shown in Fig. 3. For 50% La fraction, $c_1 = c_5$ and $c_2 = c_4$ are found as expected due to the equal amount of La and Ba.

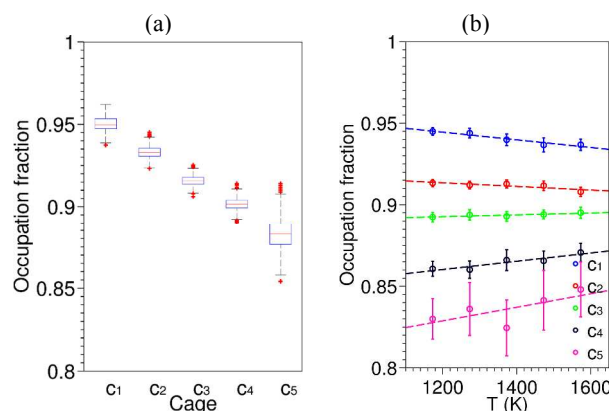


Fig. 4 Cage occupation fraction of in $\text{Ba}_{0.5}\text{La}_{0.5}\text{FeO}_{2.75}$ at 1573 K (a) and the fraction change with temperature (b).

At each output step, the occupation fraction of each cage, defined as the occupation time divided by the total simulation time, is computed. The occupation fraction of each cage type at 1573 K is reported in the boxplot in Fig. 4a, showing 10%, 25%, 50%, 75% and 90% quantiles. As shown in Fig. 4a, the occupancy fraction of c_1 is the highest and it decreases from c_2 to c_5 , indicating that, in this system, oxygen vacancies tend to be neighbor of the higher valence La^{3+} . This is counterintuitive since a higher repulsive coulombic force is expected between vacancies and La^{3+} in comparison to Ba^{2+} . Furthermore, the variation of occupation fraction in the La-rich cages is higher than that of Ba-rich cages, suggesting a low migration barrier of oxygen anions in the vicinity of La. Fig. 4b shows the mean occupation fraction with the standard deviation. With increasing temperature, the occupation fractions of Ba-rich cages c_1 and c_2 decreases, while the occupation increases for La-rich cages c_4 and c_5 , as shown in Fig. 4b. While a high occupation of Ba-rich cages is more energetically favourable, increasing the temperature excites the system to higher energy states, reducing the occupation of Ba-rich cages. The site occupancies for other La fractions are shown

in Fig. S1.

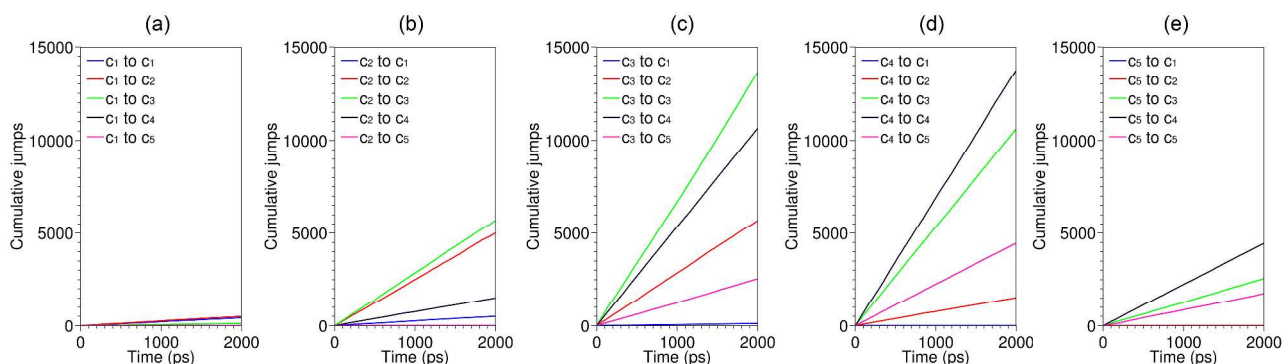


Fig. 5 Cumulative oxygen jumps from cage c_1 (a), c_2 (b), c_3 (c), c_4 (d) and c_5 (e) at 1573 K.

To study the origin of this behavior, the hopping events of oxygen atoms between cages are tracked, as shown in Fig. 5. Comparing the total cumulative jumps of Fig. 5a to the rest of Fig. 5, it is found that the number of events that oxygen jumps out of cage c_1 , formed by 4 Ba and 2 Fe, is low. This suggests that a significant energy barrier exists for the bottleneck of this cage. Fig. 5a also reveals that more jumps occur from c_1 to c_2 than from c_1 to c_1 . In fact, for the $\text{Ba}_{0.5}\text{La}_{0.5}\text{FeO}_{2.75}$, more c_2 cages exist than c_1 , as shown in Fig. 3. Moreover, although c_3 is the most common cage in this system the oxygen jumps from c_1 to c_3 are less than those from c_1 to c_2 . These observations can be attributed to the number of connections between the cages: c_1 has 4 Ba atoms and it tends to be connected to cages with more Ba. The connection number also explains why there is no jump from c_1 to c_5 , essentially a La cage. In addition, the jump events for the 25 types as in Fig. 5 but with different temperatures are shown in Fig. S2.

Furthermore, the probability of oxygen jump in a 1 ps interval, defined as the jump events over the total oxygen atom number, is shown in Fig. 6. With increasing La content, the probability generally decreases, indicating a lower diffusion rate. This is in contrast with the previous analysis, which suggests that oxygen escapes more easily from La-rich cages due to the lower migration barrier around La. The reason is that oxygen diffusivity is related to both the oxygen vacancy concentration and the migration activation energy of the vacancies. Hence, having a low migration barrier, as in the La-rich phases, does not guarantee a higher diffusion rate in the material because the vacancy concentration is lowered with increasing La. Since La substitution lowers the diffusion coefficient, the dominant effect

is attributed the lower vacancy concentration.

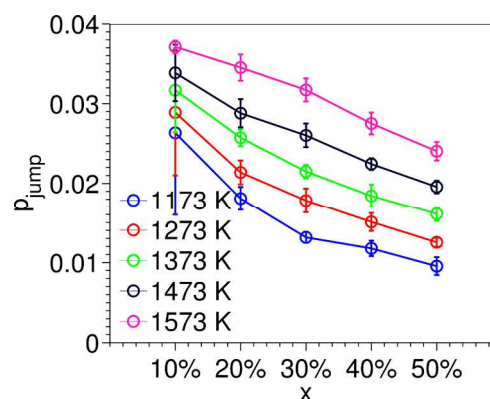


Fig. 6 The jump probability p_{jump} of oxygen atom in a 1 ps interval as a function of doping level x in $\text{Ba}_{1-x}\text{La}_x\text{FeO}_{2.5+x/2}$.

We can extract more detailed information by considering that the oxygen jumps between cages may follow different paths and thereby overcome different bottlenecks. For example, oxygen hops from c_3 (BaBaLaLa) to c_3 (BaBaLaLa) may pass through b_1 (BaBaFe), b_2 (BaLaFe) or b_3 (LaLaFe). If Ba and La have the same impact on diffusion, the number of times that oxygen passes through b_1 and b_3 should be the same for $\text{Ba}_{0.5}\text{La}_{0.5}\text{FeO}_{2.75}$. To study this bottleneck effect, we calculated the rate of jump through different bottlenecks, r_{bn} . For each bottleneck, r_{bn} is defined as the number of jumps through this bottleneck in a 1 ps interval normalized by the number of bottlenecks.

Cite this: DOI: 10.1039/c0xx00000x

www.rsc.org/xxxxxx

ARTICLE TYPE

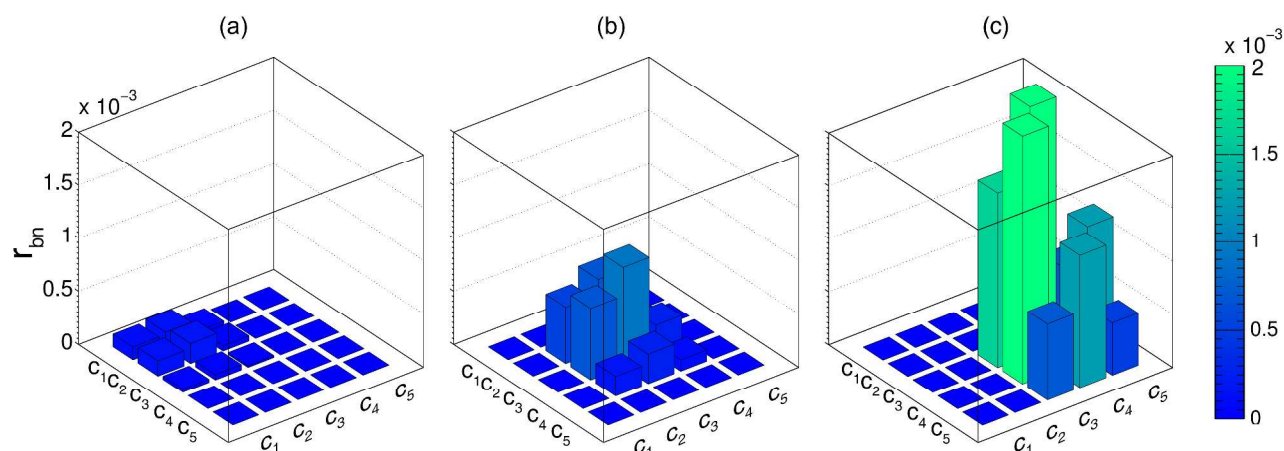


Fig. 7 Rate of oxygen jumps, r_{bn} , between the cages through b_1 (a), b_2 (b) and b_3 (c) during a 1 ps interval in $\text{Ba}_{0.5}\text{La}_{0.5}\text{FeO}_{2.75}$ at 1573 K.

Fig. 7, panels a-c, shows the rate of jump through b_1 (BaBaFe), b_2 (BaLaFe) and b_3 (LaLaFe), respectively. In Fig. 7a, the r_{bn} from the c_2 cage is higher than from the c_1 cage, indicating that the presence of La in the cage, as in c_2 , lowers the activation barrier of oxygen passing through the adjacent Ba bottleneck b_1 . In addition to this indirect influence, the presence of La in the bottlenecks themselves, as in c_3 , also lowers the migration barrier and increases the jump rate. This is evident by comparing Fig. 7a and Fig. 7c.

The analysis of above suggests that it is more difficult for oxygen to escape cages formed by lower valence Ba^{2+} cations, in comparison to those with higher valence La^{3+} . The vacancy diffusion mechanism is characterized by the activation energies, which consist of two parts, namely vacancy formation and migration. Although coulombic interactions would suggest the vacancy formation energy around Ba^{2+} to be lower, the transport bottleneck b_1 is potentially harder to overcome compared with b_2 or b_3 due to the large ionic radius of Ba^{2+} . This is easy to show when one considers the local cation arrangement at the bottleneck.⁴⁵ For example, $\text{Ba}_{0.95}\text{La}_{0.05}\text{FeO}_{3-\delta}$ has a lattice parameter of 4.0051 Å,⁸ the critical radii of the bottlenecks, as shown in Fig. 8, are 0.814 Å for b_1 , 0.898 Å for b_2 and 0.976 Å for b_3 . It is clear that the presence of Ba^{2+} reduces local lattice free volume for oxygen transport and thereby hinders the oxygen migration.

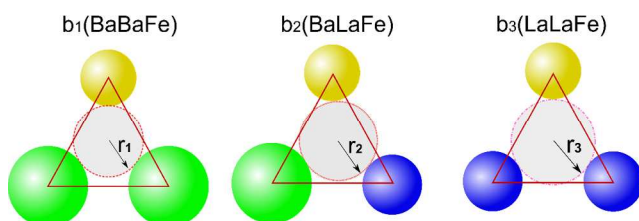


Fig. 8 Bottleneck critical radius increases from b_1 to b_2 and b_3 .

To further support the conclusions obtained from the MD simulations, we calculated the oxygen vacancy formation energies and the migration energies using DFT. The oxygen vacancy formation energy was obtained using the following formula,

$$E_{Vo} = E_{def} + \frac{1}{2}(\Delta h_{cor}^0 + E_{O_2}^{triplet}) - E_{per} \quad (1)$$

where E_{def} is computed energy with 1 oxygen vacancy, $E_{O_2}^{triplet}$ is the DFT energy for triplet O_2 , E_{per} is the energy for a perfect lattice and Δh_{cor}^0 is the energy correction term, as derived by the oxide formation energy disagreement between experiments and DFT calculations.⁴¹ A 0.72 eV energy adjustment is used to correct the overbinding problem in DFT calculations of O_2 , as shown in Fig. S3. Before computing the oxygen vacancy formation energy, we calculated the energies of different spin states. We found consistently that the ferromagnetic (FM) state to be the ground state for cubic BFO.⁴⁶ Furthermore, for La doped BFO, FM is also the ground state. The energies of various spin configurations are reported in Tab. S1.

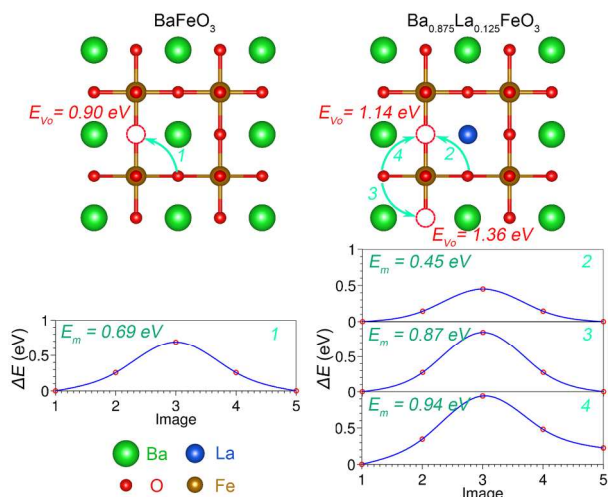


Fig. 9 The oxygen vacancy formation energies and migration energies in BFO and $\text{Ba}_{0.875}\text{La}_{0.125}\text{FeO}_3$. The arrow indicates the migration direction. Migration barrier is calculated relative to the starting position.

As shown in **Fig. 9**, in pristine BFO the cubic perovskite structure has one unique oxygen position. The vacancy formation energy is computed to be 0.90 eV, which is lower than other perovskites in the LaBO_3 ($B=\text{Fe}, \text{Mn}, \text{Co}, \text{Ni}$) series.⁴¹ One possible reason is that the Ba-containing lattice usually has a larger lattice parameter and consequently a longer Fe-O bond length, which reduces the bond strength between the transition metal and oxygen. The oxygen vacancy formation energies for the given formulae are computed to be 1.14 eV for O next to La and 1.36 eV for O away from La. Those values are higher than experimental values of vacancy formation energies of related perovskites, e.g. BSCF is 0.50 eV at $\delta = 0.52$ and $\text{Ba}_{0.5}\text{Sr}_{0.5}\text{FeO}_{2.66}$ is 0.60 eV.⁴⁷ However, they are close to 1.34–1.40 eV of $\text{Ba}_{0.5}\text{Sr}_{0.5}\text{Co}_{0.75}\text{Fe}_{0.25}\text{O}_3$.⁴⁸ The low vacancy formation energy is one of the main reasons that lead to high performance cathode materials for SOFCs. In comparison to the pristine BFO, the introduction of La increases the oxygen vacancy formation energies. As a result, a reduced concentration of oxygen vacancies is expected, leading to a lower probability of forming the lower-symmetry phases that contain substantial ordered vacancies. The decrease in vacancy concentration is also consistent with the classical charge neutrality argument: the

formation of La_{Ba}^+ is compensated by a decrease in $V_{\text{O}}^{\bullet\bullet}$ concentration. Interestingly, the vacancy formation energy near La is lower than that at an oxygen site with only Ba A-site coordination, contradicting the understanding from electrostatics since stronger repulsion is expected between La_{Ba}^+ and $V_{\text{O}}^{\bullet\bullet}$. This peculiar lower oxygen vacancy formation energy around higher valence cations was also observed in the DFT computation of $\text{La}_{1-x}\text{Sr}_x\text{Co}_{1-y}\text{Fe}_y\text{O}_3$ systems,³² and it is perhaps a consequence of the covalent bond between the cation and oxygen anion. The oxygen vacancies around La^{3+} may induce larger local lattice distortion due to smaller cation size, thereby lowering the energy of the defective system and resulting in lower vacancy formation energy. Furthermore, the lowest oxygen migration barrier reduces from 0.90 eV for the pristine BFO to 0.45 eV after substituting La, as shown in **Fig. 9**. This value is within the range of 0.42–0.52 eV in $\text{Ba}_{0.5}\text{Sr}_{0.5}\text{Co}_{0.75}\text{Fe}_{0.25}\text{O}_3$.⁴⁸ The migration barrier is comparable to the experimental value of BSCF, 0.50 eV.⁴⁹ A table with the computed values is available in the supplementary information, **Tab. S2**.

Oxygen residence analysis

The analysis of oxygen jumps provides useful information about the migration bottlenecks. The hopping events happen relatively fast and for most of the time, oxygen anions only vibrate inside the cages. In order to analyze the characteristics of oxygen in different cages, the dwell times of the oxygen atoms also need to be studied. This corresponds to determining the time for vibration as shown in **Fig. 1**. The cumulative distribution functions (CDFs) of the oxygen dwell times in cages c_1 to c_5 (corresponding to panels **a** to **e**) at different temperatures are shown in **Fig. 10**. The slower increase of CDF with dwell time at a certain cage indicates an averagely longer residence time. c_1 shows the longest oxygen dwell time at all temperatures, reflecting its ability to trap oxygen anions. This is also demonstrated in **Fig. 11**, where the average dwell time is plotted for each cage with respect to temperature variations.

The average dwell time τ_0 decreases with temperature due to increased mobility with temperature. This is also found in $\text{Ba}_{1-x}\text{La}_x\text{FeO}_{2.5+x/2}$ with $x = 0.1, 0.2, 0.3$ and 0.4.

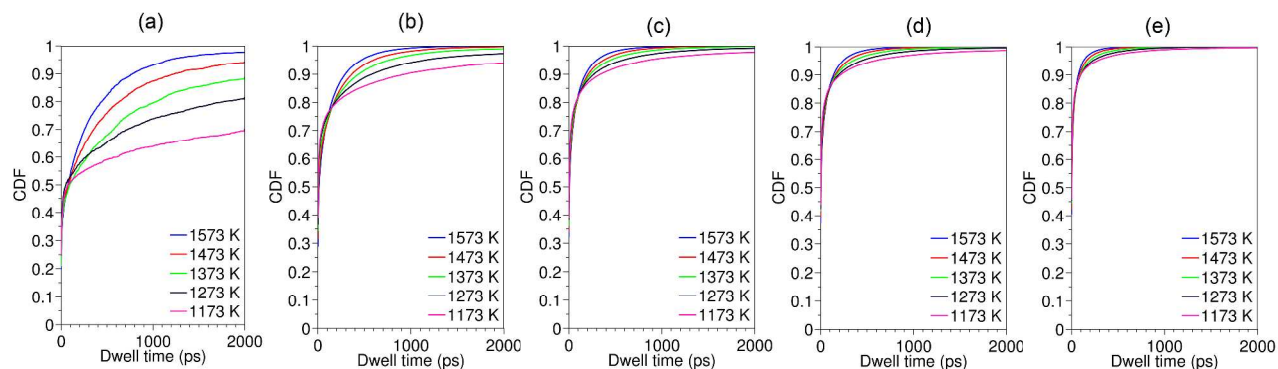


Fig. 10 Oxygen dwell time in cage c_1 (a), c_2 (b), c_3 (c), c_4 (d) and c_5 (e) for $\text{Ba}_{0.5}\text{La}_{0.5}\text{FeO}_{2.75}$ at different temperatures.

Cite this: DOI: 10.1039/c0xx00000x

www.rsc.org/xxxxxx

ARTICLE TYPE

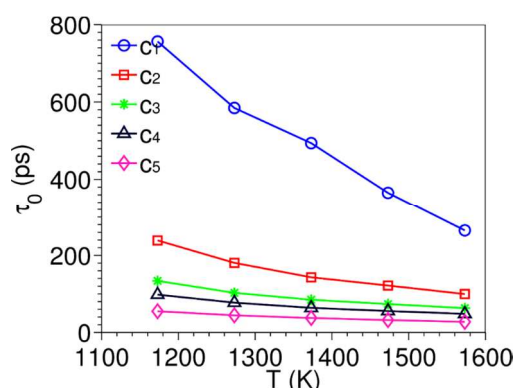


Fig. 11 Average dwell time with temperature for cage c_1 (a), c_2 (b), c_3 (c), c_4 (d) and c_5 (e) of $\text{Ba}_{0.5}\text{La}_{0.5}\text{FeO}_{2.75}$.

DFT calculations of the electronic structures

5 For mixed conductors, oxygen transport is one of the two primary properties to be considered. A good cathode material for SOFC should also have good electronic conductivity.⁴ In order to study the electronic properties, DFT calculations of the electronic structures are carried out for both pristine and La-doped BFO. It has been shown previously that the stoichiometric BFO is FM.¹³ In addition, a stable FM state is predicted for 12.5% and 25% La-substitution. The corresponding cationic configurations are shown in Fig. S4. The DOS for the ground states of different substitution levels are shown in Fig. 12.

15 While pristine BFO shows partially filled bands, La-substituted BFO exhibits semi-metallic behavior, as shown by the band opening in the minority spin states. The band gap of the minority spin state increases from 0.74 eV of BFO to 0.85 eV and 1 eV of 12.5% and 25% La-substituted BFO respectively, suggesting that with increasing the La content, the charge carrier concentration decreases, potentially leading to decreased electronic conductivity. In addition, the peaks of the O partial DOS (PDOS) in the valence band are shifted to the left of the Fermi level. Hence it is expected that the O p-band center, used as a descriptor for high temperature ORR catalysis,⁵⁰ is lowered relative to the Fermi level upon the introduction of La into the lattice. The O p-band centers are computed as -1.65 eV for BFO, -1.75 eV for $\text{Ba}_{0.875}\text{La}_{0.125}\text{FeO}_3$ and -1.99 eV for $\text{Ba}_{0.75}\text{La}_{0.25}\text{FeO}_3$. It is believed that a higher O p-band center is connected to a better ORR performance, since it indicates easier oxygen release and uptake.⁵¹ This theory has been tested on perovskites catalysts. For example BSCF has a rather high O p-band center as -1.54 eV,⁵⁰ and the other stable ORR catalyst $\text{PrBaCo}_2\text{O}_6$ (PBCO) has an O p-band center at -1.85 eV.⁵² Both materials are remarkable high temperature ORR catalysts when applied as cathodes for SOFCs. It is expected that La-substituted BFO should have a high temperature ORR performance between BSCF and PBCO. Indeed, when using these materials, the area specific resistances at 600 °C are 0.055–0.071, 0.211 and 0.86 $\Omega\text{ cm}^2$ for BSCF¹⁰, $\text{Ba}_{0.95}\text{La}_{0.05}\text{FeO}_{3-\delta}$ (BLF)⁸ and PBCO⁵³, respectively.

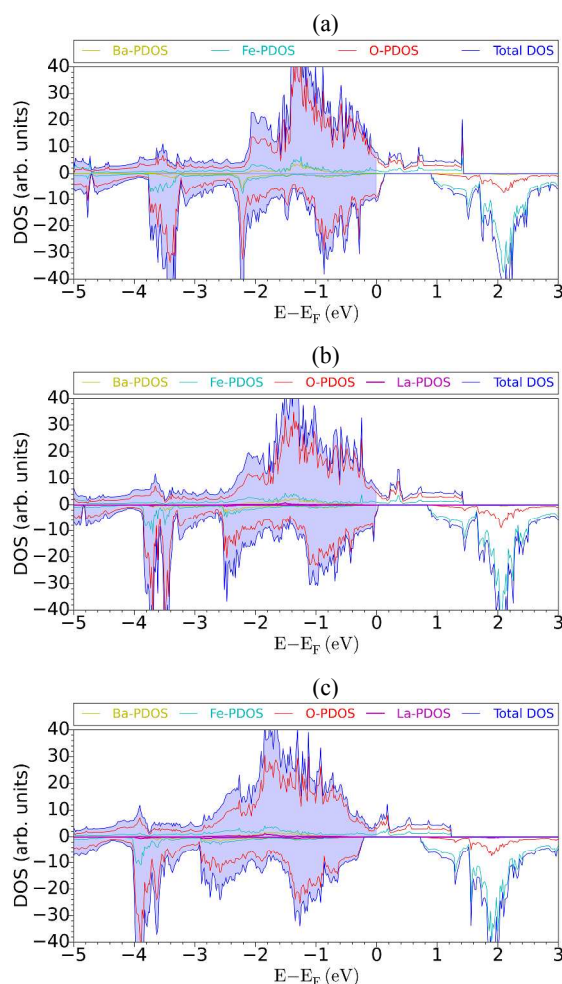


Fig. 12 DOS of BFO (a), $\text{Ba}_{0.875}\text{La}_{0.125}\text{FeO}_3$ (b) and $\text{Ba}_{0.75}\text{La}_{0.25}\text{FeO}_3$ (c).

Coincidentally, the O p-band center has also been shown as a descriptor for low temperature oxygen evolution reaction, which is key for regenerative fuel cells and metal air batteries.⁵² From a band structure perspective, a higher O p-band center usually leads to stronger hybridization between the transition metal d-band and this may be beneficial for oxygen catalysis.⁵⁴ In fact, our recent study on applying BLF-multilayer graphene as an oxygen evolution reaction (OER) catalyst has demonstrated promising OER performance of BLF,⁵⁵ which achieved 23 mA cm^{-2} at 0.60 V (vs mercury/mercury oxide reference electrode) and a Tafel slope as low as 77 mV dec^{-1} , suggesting the validity of predicting the high temperature ORR and low temperature OER performance of the materials from O p-band center descriptor. In addition, the valence state of Fe in La-substituted BaFeO_3 is between +3 and +4, as determined by the Mössbauer spectrum.⁸ The electron configuration of Fe^{4+} is $3d^4$, which forms a high spin $t_{2g}^3 e_g^1$ configuration ($\sim 4\mu_B/\text{Fe}$ as shown in Tab. S1) due to the weak lattice O ligand in the FeO_6 octahedral. As previously

reported, an e_g occupation close to 1 can be correlated to optimized OER catalytic activity due to the neither too strong nor too weak binding effect with the reaction intermediates.⁵⁶ This rationalizes why La-substituted BFO is also a good OER catalyst.

The conclusions drawn here are consistent with the predictions from the O p-band center descriptor.

Conclusions

A-site La-substituted BFO was studied by data-driven MD simulations and DFT calculations. The atomic-level analysis of oxygen jump from MD trajectories is shown to provide additional insight into the impact of local cation configuration on the oxygen diffusion. This approach complements the conventional MSD analysis, which is only capable of extracting the self-diffusion coefficient. The contribution of La is multifold. First, La decreases the oxygen vacancy concentration, suggested by the electroneutrality requirement as well as the higher vacancy formation energy calculated by DFT. This in turn reduces the probability of forming oxygen vacancy clusters or ordered vacancies, and therefore impedes the formation of vacancy-ordered low-symmetry BFO phases. Second, La lowers the activation energy for oxygen migration. This is evidenced by a higher number of jump events detected through La-containing bottlenecks. This includes a higher escape rate from La-rich oxygen cages and lower oxygen atom dwell times in La-rich cages as obtained by the data-driven MD analysis. In addition, the DFT calculations support the MD simulations in that the presence of La, lowers the activation energy of the oxygen migration pathway, in comparison to Ba. However, the average number of jumps per oxygen decreases after doping La due to the decrease in oxygen vacancy concentration. This leads to a lower diffusion coefficient. Third, the introduction of La increases the oxygen vacancy formation energy and shifts the O p-band center to lower energies referenced to the Fermi level, potentially lowering the catalytic activity of the material as an oxygen catalyst for applications in high temperature ORR as well as lower temperature OER.

Acknowledgments

The authors gratefully acknowledge the Research Grants Council of Hong Kong for support through the projects DAG12EG06 and ECS 639713. Zarah Medina Baiyee acknowledges the support of the Hong Kong PhD Fellowship Scheme.

Notes and references

^a Department of Mechanical Engineering, The Hong Kong University of Science and Technology, Hong Kong, SAR China

^b Department of Chemical and Biomolecular Engineering, The Hong Kong University of Science and Technology, Hong Kong, SAR China

* Corresponding author, tel.: +852 2358 7187, e-mail address:

francesco.ciucci@ust.hk;

1. K. Zhang, J. Sunarso, Z. Shao, W. Zhou, C. Sun, S. Wang and S. Liu, *RSC Adv.*, 2011, 1, 1661-1676.
2. S. B. Adler, *Chem. Rev.*, 2004, 104, 4791-4844.
3. A. J. Jacobson, *Chem. Mater.*, 2009, 22, 660-674.

4. C. Sun, R. Hui and J. Roller, *J. Solid State Electrochem.*, 2009, 14, 1125-1144.
5. A. Kudo and Y. Miseki, *Chem. Soc. Rev.*, 2009, 38, 253-278.
6. C. Chen, D. Chen, Y. Gao, Z. Shao and F. Ciucci, *J. Mater. Chem. A*, 2014, 2, 14154-14163.
7. K. Watanabe, M. Yuasa, T. Kida, Y. Teraoka, N. Yamazoe and K. Shimano, *Adv. Mater.*, 2010, 22, 2367-2370.
8. F. Dong, D. Chen, Y. Chen, Q. Zhao and Z. Shao, *J. Mater. Chem.*, 2012, 22, 15071-15079.
9. F. Dong, Y. Chen, D. Chen and Z. Shao, *ACS Appl. Mater. Interfaces*, 2014, 6, 11180-11189.
10. Z. Shao and S. M. Haile, *Nature*, 2004, 431, 170-173.
11. W. Zhou, R. Ran and Z. Shao, *J. Power Sources*, 2009, 192, 231-246.
12. O. Clemens, M. Gröting, R. Witte, J. M. Perez-Mato, C. Loho, F. J. Berry, R. Kruk, K. S. Knight, A. J. Wright and H. Hahn, *Inorg. Chem.*, 2014, 53, 5911-5921.
13. B. Ribeiro, M. Godinho, C. Cardoso, R. Borges and T. Gasche, *J. Appl. Phys.*, 2013, 113, 083906.
14. F. Fujishiro and T. Hashimoto, *Thermochim. Acta*, 2012, 549, 110-115.
15. T. Matsui, H. Tanaka, N. Fujimura, T. Ito, H. Mabuchi and K. Morii, *Appl. Phys. Lett.*, 2002, 81, 2764-2766.
16. C. Callender, D. P. Norton, R. Das, A. Hebard and J. D. Budai, *Appl. Phys. Lett.*, 2008, 92, 012514.
17. S. Chakraverty, T. Matsuda, N. Ogawa, H. Wadati, E. Ikenaga, M. Kawasaki, Y. Tokura and H. Hwang, *Appl. Phys. Lett.*, 2013, 103, 142416.
18. N. Hayashi, T. Yamamoto, H. Kageyama, M. Nishi, Y. Watanabe, T. Kawakami, Y. Matsushita, A. Fujimori and M. Takano, *Angew. Chem. Int. Ed.*, 2011, 123, 12755-12758.
19. Y. Suga, M. Hibino, T. Kudo and N. Mizuno, *Electrochim. Acta*, 2014, 137, 359-362.
20. D. Chen, C. Chen, F. Dong, Z. Shao and F. Ciucci, *J. Power Sources*, 2014, 250, 188-195.
21. X. Ding, X. Gao, W. Zhu, J. Wang and J. Jiang, *Int. J. Hydrogen Energy*, 2014, 39, 12092-12100.
22. T. Kida, S. Ninomiya, K. Watanabe, N. Yamazoe and K. Shimano, *ACS Appl. Mater. Interfaces*, 2010, 2, 2849-2853.
23. C. Park, T. Lee, S. Dorris and U. Balachandran, *Int. J. Hydrogen Energy*, 2013, 38, 6450-6459.
24. X. Liu, H. Zhao, J. Yang, Y. Li, T. Chen, X. Lu, W. Ding and F. Li, *J. Membr. Sci.*, 2011, 383, 235-240.
25. X. Zhu, H. Wang and W. Yang, *Solid State Ionics*, 2006, 177, 2917-2921.
26. T. Kida, A. Yamasaki, K. Watanabe, N. Yamazoe and K. Shimano, *J. Solid State Chem.*, 2010, 183, 2426-2431.
27. F. Dong, Y. Chen, R. Ran, D. Chen, M. O. Tadé, S. Liu and Z. Shao, *J. Mater. Chem. A*, 2013, 1, 9781-9791.
28. Y. Lu, H. Zhao, X. Cheng, Y. Jia, X. Du, M. Fang, Z. Du, K. Zheng and S. Konrad, *J. Mater. Chem. A*, 2015.
29. V. Goldschmidt, T. Barth, G. Lunde and W. Zachariasen, *Geochemische Verteilungsgesetze der Elemente (Oslo, 1926)*, 1926.
30. Y. Takeda, R. Kanno, M. Noda, Y. Tomida and O. Yamamoto, *J. Electrochem. Soc.*, 1987, 134, 2656-2661.

31. T. Kida, D. Takauchi, K. Watanabe, M. Yuasa, K. Shimanoe, Y. Teraoka and N. Yamazoe, *J. Electrochem. Soc.*, 2009, 156, E187-E191.
32. Y. A. Mastrikov, R. Merkle, E. A. Kotomin, M. M. Kuklja and J. Maier, *Phys. Chem. Chem. Phys.*, 2013, 15, 911-918.
33. M.-Y. Yoon, K.-J. Hwang, D.-S. Byeon, H.-J. Hwang and S.-M. Jeong, *J. Power Sources*, 2014, 248, 1085-1089.
34. C. Chen, D. Chen and F. Ciucci, *Phys. Chem. Chem. Phys.*, 2015, 17, 7831-7837.
35. S. Plimpton, *J. Comput. Phys.*, 1995, 117, 1-19.
36. M. Islam, M. Cherry and C. Catlow, *J. Solid State Chem.*, 1996, 124, 230-237.
37. C. Fisher, M. Yoshiya, Y. Iwamoto, J. Ishii, M. Asanuma and K. Yabuta, *Solid State Ionics*, 2007, 177, 3425-3431.
38. G. Kresse and J. Furthmüller, *Comput. Mater. Sci.*, 1996, 6, 15-50.
39. G. Kresse and J. Furthmüller, *Phys. Rev. B*, 1996, 54, 11169.
40. L. Wang, T. Maxisch and G. Ceder, *Phys. Rev. B*, 2006, 73, 195107.
41. Y.-L. Lee, J. Kleis, J. Rossmeisl and D. Morgan, *Phys. Rev. B*, 2009, 80, 224101.
42. P. E. Blöchl, O. Jepsen and O. K. Andersen, *Phys. Rev. B*, 1994, 49, 16223.
43. G. Henkelman, B. P. Uberuaga and H. Jónsson, *J. Chem. Phys.*, 2000, 113, 9901-9904.
44. K. Momma and F. Izumi, *J. Appl. Crystallogr.*, 2011, 44, 1272-1276.
45. J. Kilner and R. Brook, *Solid State Ionics*, 1982, 6, 237-252.
46. Z. M. Baiyee, C. Chen and F. Ciucci, *Phys. Chem. Chem. Phys.*, 2015, DOI: 10.1039/C5CP02694F.
47. L. Wang, R. Merkle, G. Cristiani, B. Stuhlhofer, H.-U. Habermeier and J. Maier, *ECS Trans.*, 2008, 13, 85-95.
48. E. Kotomin, Y. A. Mastrikov, M. Kuklja, R. Merkle, A. Roytburd and J. Maier, *Solid State Ionics*, 2011, 188, 1-5.
49. L. Wang, R. Merkle and J. Maier, *J. Electrochem. Soc.*, 2010, 157, B1802-B1808.
50. Y.-L. Lee, J. Kleis, J. Rossmeisl, Y. Shao-Horn and D. Morgan, *Energy Environ. Sci.*, 2011, 4, 3966-3970.
51. M. H. Lankhorst, H. Bouwmeester and H. Verweij, *Phys. Rev. Lett.*, 1996, 77, 2989.
52. A. Grimaud, K. J. May, C. E. Carlton, Y.-L. Lee, M. Risch, W. T. Hong, J. Zhou and Y. Shao-Horn, *Nat. Commun.*, 2013, 4.
53. D. Chen, R. Ran, K. Zhang, J. Wang and Z. Shao, *J. Power Sources*, 2009, 188, 96-105.
54. W. T. Hong, M. Risch, K. A. Stoerzinger, A. Grimaud, J. Suntivich and Y. Shao-Horn, *Energy Environ. Sci.*, 2015, 8, 1404-1427.
55. H. Zhao, C. Chen, D. Chen, M. Saccoccio, J. Wang, Y. Gao, T. H. Wan and F. Ciucci, *Carbon*, 2015, 90, 122-129.
56. J. Suntivich, K. J. May, H. A. Gasteiger, J. B. Goodenough and Y. Shao-Horn, *Science*, 2011, 334, 1383-1385.